Journal of Biomechanics 53 (2017) 111–119

Contents lists available at ScienceDirect

Journal of Biomechanics

journal homepage: www.elsevier.com/locate/jbiomech
www.JBiomech.com

Twente spine model: A complete and coherent dataset for musculo-skeletal modeling of the lumbar region of the human spine

Riza Bayoglu [a,*], Leo Geeraedts [b], Karlijn H.J. Groenen [c], Nico Verdonschot [a,c], Bart Koopman [a], Jasper Homminga [a]

[a] Department of Biomechanical Engineering, University of Twente, P.O. Box 217, 7500 AE Enschede, The Netherlands
[b] Radboud University Medical Center, Department of Anatomy, Nijmegen, The Netherlands
[c] Radboud University Medical Center, Radboud Institute for Health Sciences, Orthopaedic Research Laboratory, Nijmegen, The Netherlands

ARTICLE INFO

Article history:
Accepted 5 January 2017

Keywords:
Lumbar spine
Cadaver
Musculo-skeletal model
Muscles
Sarcomere length

ABSTRACT

Musculo-skeletal modeling can greatly help in understanding normal and pathological functioning of the spine. For such models to produce reliable muscle and joint force estimations, an adequate set of musculo-skeletal data is necessary. In this study, we present a complete and coherent dataset for the lumbar spine, based on medical images and dissection measurements from one embalmed human cadaver. We divided muscles into muscle-tendon elements, digitized their attachments at the bones and measured morphological parameters. In total, we measured 11 muscles from one body side, using 96 elements. For every muscle element, we measured three-dimensional coordinates of its attachments, fiber length, tendon length, sarcomere length, optimal fiber length, pennation angle, mass, and physiological cross-sectional area together with the geometry of the lumbar spine. Results were consistent with other anatomical studies and included new data for the serratus posterior inferior muscle. The dataset presented in this paper enables a complete and coherent musculo-skeletal model for the lumbar spine and will improve the current state-of-the art in predicting spinal loading.

1. Introduction

The combination of flexibility and rigidity that characterizes the spine makes it vulnerable to a range of mechanical and medical problems, and it is therefore an important area for biomechanical research. Most spine research has focused on the lumbar spine with a special focus on low back pain (McGill, 1992; Alireza et al., 2011; Zander et al., 2015; Putzer et al., 2016) and disc herniation (Wilke et al., 2016). Despite high quality research on the lumbar spine, our understanding of its *in-vivo* mechanical function remains limited due to its complex structure. Musculo-skeletal models of the lumbar spine would enable clinical insights into its functioning, and allow answering *what if* questions (Blemker et al., 2007).

The capability of a muscle to produce torques at the joints is directly related to its moment arms, and thus to its origin and insertion, and to its strength (Vasavada et al., 1998). Therefore, representation of muscles in musculo-skeletal models demands special care to simulate true anatomy and realistic *in-vivo* muscle function. In the lower extremity, Carbone et al. (2012) demonstrated that small differences in muscle attachments may markedly affect muscle moment arms, and, thus affect muscle force predictions considerably. Furthermore, morphological parameters such as optimal fiber length, tendon length and physiological cross-sectional area, are critical inputs into musculo-skeletal models (Kamibayashi and Richmond, 1998). In short, accuracy of modeling lines-of-action and morphological parameters determine muscle activation levels and have significant effects on the output of a musculo-skeletal model.

Currently there is no musculo-skeletal dataset which enables the development of a complete and coherent model for the lumbar spine. None of the previous studies quantified muscle attachments at the bones and measured complete morphological parameters for *all* muscles of the lumbar spine (Bogduk et al., 1992a, 1992b, 1998; Macintosh and Bogduk, 1991; Macintosh et al., 1986; Delp et al., 2001; Phillips et al., 2008). Instead, they typically focused on a smaller part of the lumbar spine and presented anatomical drawings to illustrate muscle attachments. Subsequently, current musculo-skeletal models require piecing together data from these studies and making assumptions when data does not exist. Consequently, such models will require complex scaling between the geometries and the muscle architectures of the cadaveric specimens (de Zee et al., 2007; Arjmand et al., 2009; Christophy et al., 2012; Ignasiak et al., 2016). This approach may then result in a

* Corresponding author. Fax: +31 53 489 2287.
E-mail address: r.bayoglu@hotmail.com (R. Bayoglu).

http://dx.doi.org/10.1016/j.jbiomech.2017.01.009
0021-9290/

musculo-skeletal system that never really existed (Borst et al., 2011). Therefore, a musculo-skeletal model based on *one* complete and coherent dataset—obtained from *one* body—would further improve our understanding of the human spine and is, thus, a better approach for clinical use (Klein Horsman et al., 2007). The aim of our work is to obtain a complete and coherent anatomical dataset for the entire human spine, but in this paper we focus on the lumbar spine alone. This dataset includes segmented bone surfaces, three-dimensional coordinates of muscle attachment sites, bony wrapping surfaces and morphological muscle parameters from a single human cadaver.

2. Materials and methods

2.1. Cadaveric specimen

An embalmed human cadaver body (79 years-old, male, height: 154 cm, mass: 51 kg) was obtained with institutional approval from Radboud university medical center. The cause of death was Alzheimer. We noticed that the fifth lumbar vertebra was fused to the sacrum. In the cadaver, we distinguished 33 bones: twelve thoracic and four lumbar vertebrae, twelve ribs, sternum, humerus, femur, sacrum and pelvis.

2.2. Medical imaging

Prior to dissection, we acquired full body supine computed tomography (CT) images (Siemens SOMATOM Sensation 64, Siemens AG, Munich, Germany, voxel size 0.977 mm x 0.977 mm x 1 mm).

2.3. Cadaveric measurements

We measured muscles of the lumbar spine from the right side of the trunk, therefore we removed complete skin and subcutaneous fat on this side. Subsequently, we inserted reference tube-screw connectors (see Fig. 1a) in the bones under the guidance of a C-arm device (Phillips BV 29). These connectors were used to construct *temporary local reference frames* in the bones enabling the consistent alignment of the optical reference tool between position measurement sessions. To strengthen the fixation between the bones and the connectors, Polymethylmethacrylate (PMMA) was poured through the screw guide holes. The positions of muscle attachments in three-dimensions with respect to the corresponding reference frames of the bones were measured using the NDI Hybrid Polaris Spectra tracking system. Because it was not possible to insert the connectors in the ribs, muscles that had attachments to the ribs were measured with respect to other bones nearby (for example, an attachment site at the twelfth rib was measured with respect to the reference frame of the twelfth vertebra). A graphical user interface was developed in Matlab R2014b to communicate with the tracking system and was utilized to properly record the measurements. Prior to the experiment, we assessed the accuracy of using these connectors. We found a position error of 0.331 ± 0.391 mm for measuring a single attachment point.

2.3.1. Muscle attachment sites

After identification of a target muscle, fat at the intramuscular connections was removed, and the muscle was divided into several muscle-tendon elements to represent its function more accurately in the musculo-skeletal model. The number of elements (functionally different parts of a muscle) was decided by using a previously described method (Breteler et al., 1999). The dissections were performed by an experienced anatomist. After locating the tendons at origin and insertion of the muscle elements, colored beads were used to mark the attachments of the

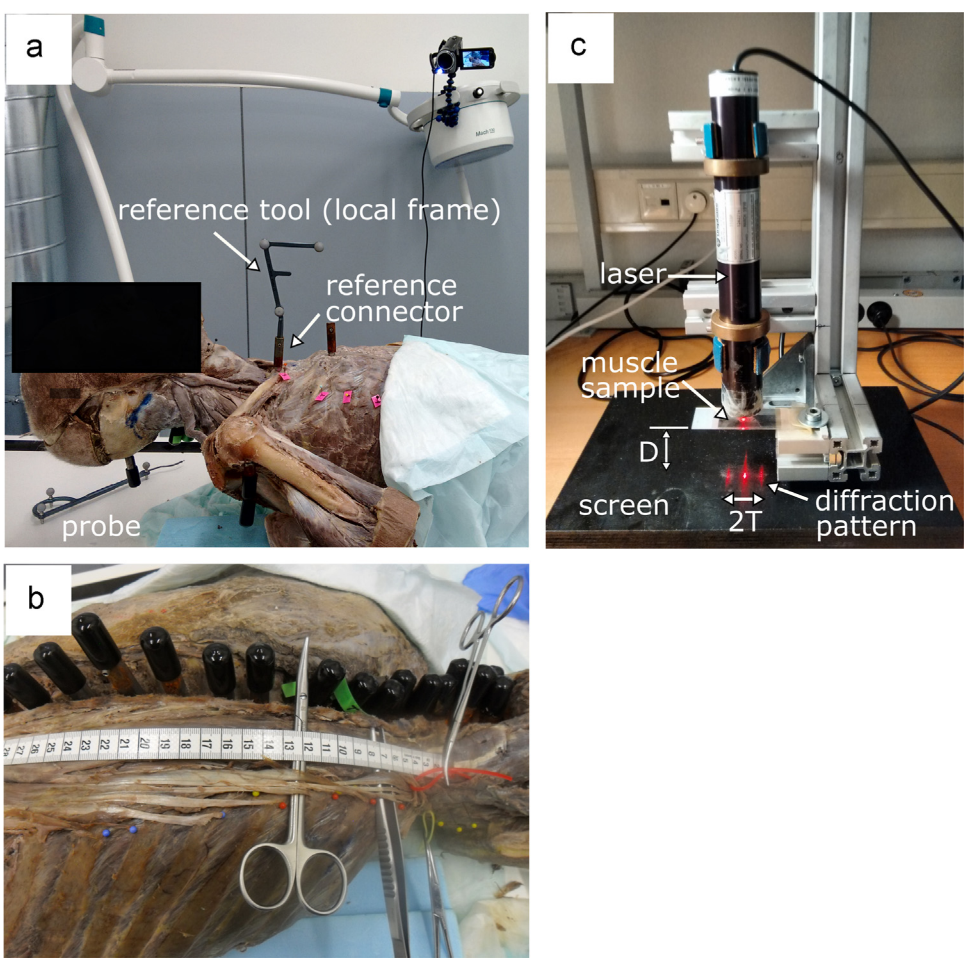

Fig. 1. (a) An instance during position measurements. (b) Locating attachments of Erector Spinae muscle group. (c) Laser diffraction set-up used for sarcomere length measurements.

elements (see Fig. 1b). Subsequently, we resected muscle elements and measured positions of their attachments at origin and insertion. We also measured the positions of via points (locations where a muscle is constrained to move) for elements with a curved lines-of-action. Depending on the size and shape of the muscles, we measured the attachments in one of the three geometrical forms, *point*, *line* or *surface* (see Fig. 2). Finally, we labeled the muscle elements and stored them in 2% formaldehyde solution until the measurement of morphological parameters.

The resection procedure differed slightly for iliocostalis, longissimus, and multifidus muscles. Dividing these muscles into elements *in-situ* was not possible due to superficial and deep layers of muscle fibers. First, positions of attachments (where possible) at the bones were measured, and the entire muscle was resected afterwards. Later, they were micro-dissected and were divided into elements as done in previous anatomical studies (Macintosh et al., 1986; Macintosh and Bogduk, 1987). In addition, measuring the attachments of the psoas major muscle was impossible, as this muscle has its origins inside the abdominal cavity on the anterior side, which prevented the optical tools from being seen by the camera. We identified and noted its origins at the bones and later modeled their lines-of-action based on the study by Bogduk et al. (1992b).

2.3.2. Muscle morphological parameters

For every element, we measured the following morphological muscle parameters: fiber length, tendon length, sarcomere length, optimal fiber length, pennation angle, mass, and physiological cross-sectional area. Prior to measuring these parameters, remaining fat and connective tissue on the surface of the muscle elements were carefully removed.

Pennation angle was measured by using a protractor (we neglected to measure the angles below 10°). Subsequently, the muscle element was placed on a flat table, and its musculo-tendon length (tendon-muscle-tendon length) between most proximal and distal ends was measured by using a ruler with a resolution of 0.5 mm. Depending on the size of an element, we measured the lengths of up to six representative fibers to calculate an average fiber length for that element. Next, tendons were cut at both ends, and an average tendon length was calculated by subtracting average fiber length, multiplied by the cosine of the pennation angle, from measured musculo-tendon length. Then, we weighed the muscle elements (muscle fibers) by using a scale which had a resolution of 0.01 g. Elements were wiped with tissue to remove excess fluid before weighing. Due to the complex tendinous connections of the abdomen muscles, obliquus externus abdominis and obliquus internus abdominis, we measured their tendon lengths while the muscles were still intact.

Average sarcomere length for every muscle was calculated by using the laser diffraction method (Cross et al., 1981). For this, a vertical laser set-up which employed a Helium-Neon laser with a beam diameter of 2 mm and a wavelength of 632.8 nm was used (see Fig. 1c). A constant distance (D=55 mm) was maintained between the samples and reading screen throughout the measurements. We measured the distance between the first diffraction bands (2 T in Fig. 1c) with a digital caliper (with a resolution of 0.01 mm) and calculated sarcomere length (SL, in μm) from this distance by using Eq. (1):

$$\mathrm{SL} = \frac{632.8 \times 10^{-3} \times D \times \sqrt{\left(\frac{T}{D}\right)^2 + 1}}{T} \quad (1)$$

Six to ten samples—consisting of one to five muscle fibers—were peeled from the representative element under an operation microscope and were used for the measurements. Samples were prepared from proximal end, distal end, and middle of the element. If the standard deviation of six samples exceeded 0.25 μm, we included up to four more samples taken between the proximal end and middle, and distal end and middle of the element. For each sample, we performed three sarcomere length measurements (at either ends and middle of the sample) and calculated the mean of three measurements. Subsequently, the average sarcomere length of a muscle was calculated from all the samples.

The optimal fiber length of an element (in mm) was calculated by using Eq. (2),

$$\ell_o^f = \frac{\ell^f}{\ell^s} \times 2.7 \quad (2)$$

where ℓ^f is the average fiber length and ℓ^s is the average sarcomere length of the muscle. We assumed an optimal sarcomere length of 2.7 μm for skeletal muscles (Breteler et al., 1999).

The volume of muscle elements was calculated by assuming a density of 1.0576 g/cm^3 for muscle tissue (Breteler et al., 1999). Moreover, physiological cross-sectional area (PCSA, in cm^2) was calculated according to Eq. (3),

$$\mathrm{PCSA} = \frac{\mathrm{mass} \times \cos(\alpha)}{\rho \times \ell_o^f} \quad (3)$$

where α is the pennation angle, ρ is the muscle density, mass is the mass of the element, and ℓ_o^f is the optimal fiber length. In line with Brown et al. (2011), for the rectus abdominis PCSA was calculated as the largest measured regional PCSA and was distributed among its elements with respect to their masses. Fiber lengths were summed for all regions.

2.4. Processing of muscle attachments

We manually segmented CT images into stereolithography (STL) geometry files (Mimics 18.0 Materialise N.V., Leuven, Belgium). The iterative closest point algorithm was used to register point clouds (scanned over the bone surfaces) with the STL files (Besl and McKay, February 1992). See Appendix A.1 for more details. After registration, muscle attachments (measured with respect to the *temporary local reference frames* of the bones) were transformed to the *global reference frame* defined by the CT scanner. In the global reference frame, x-, y-, and z-axes point cranially, posteriorly, and laterally (to the left), respectively.

For line-shaped attachments, a polynomial of third degree was fit through the measured points. Subsequently, n equidistant points (n is the number of elements that share an attachment site together) were calculated on the fitted polynomial curve as to represent the attachments of the elements (Pellikaan et al., 2014). The point-shaped attachments did not require further processing. For surface-shaped attachments, first a plane was fitted through the measured points. The measured points were projected onto the fitted plane, and a surface area was interpolated through the projected points. Later, the centroids of the n equi-areal parts of the surface were calculated to represent the attachments for the elements (Pellikaan et al., 2014), referring to der Helm et al. (1992). Finally, all the calculated attachments were either projected on the surface of the STL files or left intact, depending on whether an element attached to only one bone or spanned between multiple bones, respectively.

Furthermore, we graphically estimated wrapping surfaces—from the geometry of the spine and measured point clouds over the structures that muscles wrap—in the AnyBody Modeling System™ version. 6.0.4 (AnyBody Technology A/S, Aalborg, Denmark). Depending on the shape of a surface, either a cylinder or an ellipsoid was estimated. See Appendix A.2 for details.

3. Results

The complete list of measured muscle elements is given in Table 1. In total, we measured 11 muscles from one side of the body using 96 muscle elements. For every element, we obtained the coordinates of its attachments at origin and insertion together with the morphological parameters: fiber length, sarcomere length, optimal fiber length, tendon length, pennation angle, mass, and physiological cross-sectional area (PCSA). Individual PCSAs were relatively small, the largest being 2.74 cm^2 for an element of the psoas major. Total muscle PCSAs ranged from 2.07 cm^2 for the serratus posterior inferior to 18.50 cm^2 for the longissimus thoracis. Mean sarcomere lengths ranged from 2.14 μm for the internal oblique to 3.57 μm for the longissimus thoracis. Fiber length ranged from 2.0 cm for an element of the transversus abdominis to 26.3 cm for an element of the rectus abdominis. Mean optimal fiber lengths ranged from 4.0 cm for multifidus to 25.1 cm for the rectus abdominis. Tendon lengths for the thoracic component of the longissimus thoracis were very long, ranging from 7.4 cm to 26.6 cm, while its lumbar component had relatively short tendon lengths. The definitions of wrapping surfaces can be found in Appendix A.2, and the coordinates of via points can be found in Appendix A.3 both as digital appendices. All the bones with reconstructed muscle lines-of-action were visualized in the AnyBody Modeling System™ ver. 6.0.4 (AnyBody Technology A/S, Aalborg, Denmark) and are depicted in Fig. 3.

4. Discussion

In this study we measured a musculo-skeletal dataset for the lumbar region of the trunk, consisting of the coordinates of muscle attachments, three-dimensional geometry of the bones (in the form of STL files), and morphological parameters of muscles. We noticed that most muscles had curved lines-of-action. Therefore, the coordinates of via points and the definitions of wrapping surfaces were provided in addition to their origins and insertions. For every muscle element, we provided morphological parameters: fiber length, tendon length, sarcomere length, optimal fiber length, pennation angle, mass, and PCSA. These parameters

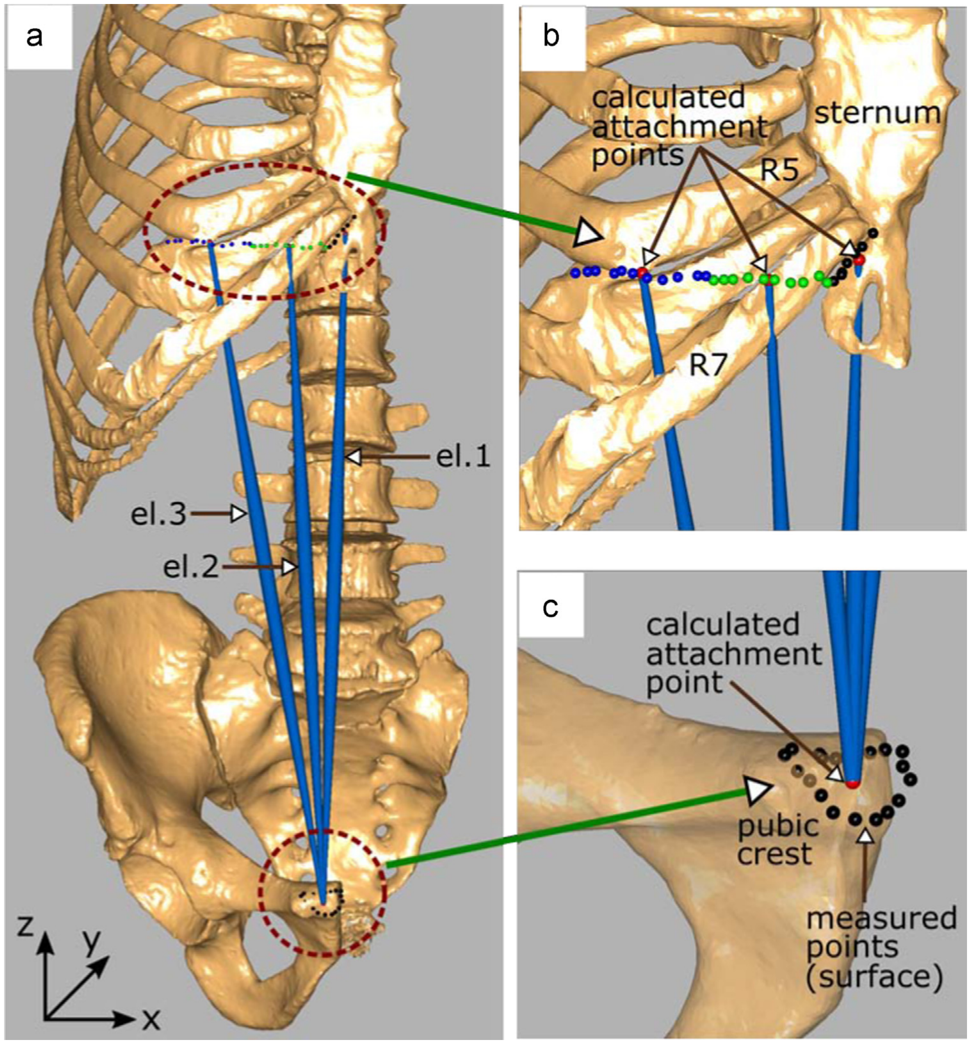

Fig. 2. (a) Illustration of the geometrical forms used to classify line and surface-shaped muscle attachment sites. Rectus abdominis muscle is used for this illustration. (b) The insertions of this muscle was measured in line form. Black, green, and the blue dots represent the measured attachment points for the elements 1, 2, and 3, respectively. Three red dots indicate calculated attachment points for these elements. Note that n is equal to 1 in this case since the attachments of each element were measured separately. (c) Differently, the origin of the muscle was measured in surface form (black dots), and the red dot indicates the calculated attachment point (the centroid of the surface). Since this surface was considerably small, we opted to define one common origin for the all the elements ($n = 1$). (For interpretation of the references to color in this figure caption, the reader is referred to the web version of this paper.)

facilitate better simulation of muscle mechanics and hence will improve these types of models (Zajac, 1989). As the dataset was obtained from a single cadaver, it is complete and coherent and omits the uncertainties associated with combining musculo-skeletal data from different specimens and measurement methods (Dao and Tho, 2015; Carbone et al., 2015). Additionally, it includes new data for the serratus posterior inferior muscle. As such, the dataset enables construction of a complete and coherent musculo-skeletal model for the lumbar spine. With this dataset we aim to contribute to an improvement of the state-of-the art in predicting lumbar spinal loading. This dataset is freely available to be used for non-commercial purposes through https://www.utwente.nl/en/et/bw/research/projects/twentespinemodel, upon the acceptance of our research license agreement.

During measurements we observed some interesting differences compared to previous studies. Firstly, we did not encounter the lumbar fascicles of iliocostalis lumborum as seen by Macintosh and Bogduk (1987), but encountered the lumbar fascicles of longissimus thoracis. Our findings were thus more in line with those of Bustami (1986) who did not find any attachment of the iliocostalis to the lumbar transverse processes. Secondly, the thoracic component of the longissimus thoracis only had attachments at ribs 5–9, whereas Macintosh and Bogduk (1987) found connections at ribs 6–12. Thirdly, we did not find any bundles of psoas major originating from the L1L2 disc nor from the L4L5 disc, but we observed bundles originating from the L2 and L3 vertebrae. Small variations were also found for other muscles. These disparities are most likely explained by the variations in the anatomy of the specimens and the differences in the techniques.

This research had several limitations. Firstly, we noticed a slight scoliosis around the cadaver's neck, and after dissection of the muscles we discovered that L5 vertebra was fused to the sacrum (Mahato, 2013). One would not expect an effect on the muscle architecture in the lumbar region due to the scoliosis, however the same may not be true due to the sacralization. The muscles between the L5 and sacrum are thus most likely different in this cadaver. Secondly, we dissected only on the right side of the specimen. When a model is built upon this dataset, this requires assumptions about the skeletal geometry and the muscle architecture on the left side. Although it is simply convenient to build a left-right symmetrical model, no one ever has a perfectly symmetrical musculo-skeletal system. Thirdly, measured morphological parameters may not represent *in-vivo* function accurately. Cutts (1988) reported no significant decrease in muscle fiber

Table 1

Per muscle element: element number (#), fiber length (ℓ^f), sarcomere length (ℓ^s), optimal fiber length (ℓ^f_o), tendon length (ℓ^t), pennation angle (α), physiological cross-sectional area (PCSA), and coordinates of attachments at origin and insertion with respect to the global reference frame defined by the CT scanner[1,2,3].

Muscle	#	ℓ^f (mm)	ℓ^s (μm)	ℓ^f_o (mm)	ℓ^t (mm)	α (deg)	Mass (g)	PCSA(cm^2)	Origin (bone)	Form	Position (m)			Insertion (bone)	Form	Position (m)		
											x	y	z			x	y	z
Obliquus externus abdominis	1	71.1	2.82	68.2	35.9	0	8.18	1.13	Pelvis	Line	−0.1262	−0.1046	0.7301	R11	Line	−0.1167	−0.0965	0.7811
Obliquus externus abdominis	2	103.8	2.82	99.6	95.2	0	19.04	1.81	Pelvis	Line	−0.1365	−0.1401	0.7092	R10	Surface	−0.1253	−0.1010	0.8197
Obliquus externus abdominis	3	125.6	2.82	120.4	172.4	0	20.29	1.59	Pelvis	Line	−0.1233	−0.1700	0.6836	R9	Surface	−0.1312	−0.1159	0.8462
Obliquus externus abdominis	4	131.7	2.82	126.2	153.4	0	16.59	1.24	Linea alba	Line	0.0000	−0.2142	0.6541	R8	Surface	−0.1368	−0.1413	0.8652
Obliquus externus abdominis	5	96.7	2.82	92.7	120.7	0	12.76	1.30	Linea alba	Line	0.0000	−0.2240	0.7226	R7	Line	−0.1324	−0.1707	0.8752
Obliquus externus abdominis	6	58.5	2.82	56.1	137.7	0	9.51	1.60	Linea alba	Line	0.0000	−0.2316	0.7841	R6	Line	−0.1208	−0.1893	0.8982
Obliquus externus abdominis	7	56.2	2.82	53.9	83.7	0	1.53	0.27	Linea alba	Line	0.0000	−0.2407	0.8538	R5	Line	−0.1109	−0.1952	0.9254
Iliocostalis lumborum	1	81.5	2.81	78.3	23.5	0	15.54	1.88	Pelvis	Surface	−0.0601	−0.0522	0.7270	R11	Point	−0.0776	−0.0601	0.8403
Iliocostalis lumborum	2	100.4	2.81	96.4	59.6	0	18.99	1.86	Pelvis	Surface	−0.0551	−0.0475	0.7198	R10	Point	−0.0766	−0.0504	0.8878
Iliocostalis lumborum	3	106.7	2.81	102.4	108.3	0	7.87	0.73	Pelvis	Surface	−0.0503	−0.0437	0.7122	R9	Point	−0.0741	−0.0495	0.9221
Iliocostalis lumborum	4	98.0	2.81	94.1	172.0	0	5.95	0.60	Pelvis	Surface	−0.0466	−0.0406	0.7057	R8	Point	−0.0800	−0.0513	0.9646
Iliocostalis lumborum	5	114.7	2.81	110.1	202.3	0	5.84	0.50	Pelvis	Surface	−0.0440	−0.0387	0.6989	R7	Point	−0.0798	−0.0556	0.9789
Iliocostalis lumborum	6	114.7	2.81	110.1	235.3	0	5.84	0.50	Pelvis	Surface	−0.0420	−0.0370	0.6941	R6	Point	−0.0709	−0.0610	1.0160
Obliquus internus abdominis	1	36.8	2.14	46.4	19.8	0	8.08	1.65	Pelvis	Line	−0.0923	−0.0777	0.7381	R11	Line	−0.1170	−0.1012	0.7781
Obliquus internus abdominis	2	55.5	2.14	70.1	29.5	0	13.23	1.78	Pelvis	Line	−0.1194	−0.0997	0.7329	R10	Line	−0.1216	−0.1643	0.7738
Obliquus internus abdominis	3	88.5	2.14	111.8	135.0	0	27.09	2.29	Pelvis	Line	−0.1345	−0.1294	0.7208	Linea alba	Line	0.0000	−0.2365	0.8387
Obliquus internus abdominis	4	57.9	2.14	73.1	117.1	0	8.92	1.15	Pelvis	Line	−0.1275	−0.1628	0.6931	Linea alba	Line	0.0000	−0.2320	0.7729
Obliquus internus abdominis	5	51.5	2.14	65.0	87.7	0	5.41	0.79	Pelvis	Line	−0.1135	−0.1783	0.6720	Linea alba	Line	0.0000	−0.2237	0.7100
Obliquus internus abdominis	6	56.5	2.14	71.4	64.5	0	4.83	0.64	Pelvis	Line	−0.0973	−0.1797	0.6399	Linea alba	Line	0.0000	−0.2146	0.6513
Latissimus dorsi	1	229.7	2.26	274.6	123.8	0	70.14	2.42	Pelvis	Line	−0.0775	−0.0647	0.7360	Humerus	Line	−0.1382	−0.1698	1.0543
Latissimus dorsi	2	228.8	2.26	273.5	196.6	35	37.88	1.07	L2	Line	−0.0034	−0.0461	0.7770	Humerus	Line	−0.1362	−0.1652	1.0503
Latissimus dorsi	3	209.7	2.26	250.7	120.3	0	37.62	1.42	T11	Line	−0.0046	−0.0373	0.8546	Humerus	Line	−0.1365	−0.1616	1.0470
Latissimus dorsi	4	190.5	2.26	227.7	112.0	0	19.27	0.80	T9	Line	−0.0055	−0.0347	0.9029	Humerus	Line	−0.1375	−0.1588	1.0430
Latissimus dorsi	5	171.3	2.26	204.8	103.7	0	9.74	0.45	T7	Line	−0.0077	−0.0364	0.9558	Humerus	Line	−0.1385	−0.1566	1.0400
Longissimus thoracis	1	93.0	3.57	70.3	225.3	0	6.49	0.87	L4	Line	−0.0070	−0.0475	0.7327	R5	Point	−0.0425	−0.0749	1.0410
Longissimus thoracis	2	80.7	3.57	61.0	215.8	0	0.77	0.12	Sacrum	Line	−0.0073	−0.0370	0.6866	R8	Point	−0.0403	−0.0558	0.9749
Longissimus thoracis	3	85.0	3.57	64.3	203.7	0	2.31	0.34	Sacrum	Line	−0.0073	−0.0370	0.6866	R8	Point	−0.0454	−0.0496	0.9657
Longissimus thoracis	4	105.3	3.57	79.6	217.7	0	2.51	0.30	L5	Line	−0.0081	−0.0445	0.7140	R6	Point	−0.0492	−0.0653	1.0247
Longissimus thoracis	5	87.0	3.57	65.8	204.5	0	1.94	0.28	Sacrum	Line	−0.0040	−0.0270	0.6551	R9	Point	−0.0456	−0.0473	0.9380
Longissimus thoracis	6	77.0	3.57	58.2	240.4	0	1.05	0.17	Sacrum	Line	−0.0073	−0.0398	0.6919	R7	Point	−0.0513	−0.0552	0.9990
Longissimus thoracis	7	27.0	3.57	20.4	12.0	0	4.86	2.25	Sacrum	Line	−0.0391	−0.0559	0.7002	L5	Point	−0.0367	−0.0690	0.7240
Longissimus thoracis	8	42.0	3.57	31.8	18.0	0	5.69	1.69	Pelvis	Line	−0.0406	−0.0422	0.6979	L4	Point	−0.0338	−0.0784	0.7398
Longissimus thoracis	9	64.0	3.57	48.4	20.0	0	7.90	1.54	Pelvis	Line	−0.0412	−0.0406	0.6962	L3	Point	−0.0263	−0.0796	0.7652
Longissimus thoracis	10	91.7	3.57	69.3	33.3	0	12.57	1.71	Pelvis	Line	−0.0412	−0.0406	0.6962	L2	Point	−0.0247	−0.0786	0.7876
Longissimus thoracis	11	109.3	3.57	82.7	55.7	0	22.89	2.62	Pelvis	Line	−0.0412	−0.0406	0.6962	L1	Point	−0.0240	−0.0703	0.8157
Longissimus thoracis	12	135.3	3.57	102.4	73.8	0	15.52	1.43	Sacrum	Line	−0.0445	−0.0426	0.6467	T12	Point	−0.0220	−0.0603	0.8448
Longissimus thoracis	13	87.7	3.57	66.3	150.2	0	11.41	1.63	Sacrum	Line	−0.0398	−0.0397	0.6417	T11	Point	−0.0268	−0.0529	0.8732
Longissimus thoracis	14	102.8	3.57	77.7	168.6	0	4.08	0.50	Sacrum	Line	−0.0253	−0.0349	0.6400	T10	Point	−0.0295	−0.0476	0.9072
Longissimus thoracis	15	63.5	3.57	48.0	216.3	0	1.43	0.28	Sacrum	Line	−0.0040	−0.0270	0.6551	T9	Point	−0.0299	−0.0444	0.9292
Longissimus thoracis	16	68.3	3.57	51.6	210.4	0	1.80	0.33	Sacrum	Line	−0.0073	−0.0370	0.6866	T8	Point	−0.0314	−0.0481	0.9605
Longissimus thoracis	17	57.8	3.57	43.7	241.2	0	1.18	0.26	Sacrum	Line	−0.0073	−0.0398	0.6919	T7	Point	−0.0316	−0.0531	0.9853
Longissimus thoracis	18	82.3	3.57	62.3	224.7	0	2.43	0.37	L5	Line	−0.0081	−0.0445	0.7140	T6	Point	−0.0320	−0.0618	1.0133
Longissimus thoracis	19	76.3	3.57	57.7	237.6	0	2.54	0.42	L4	Line	−0.0070	−0.0475	0.7327	T5	Point	−0.0336	−0.0752	1.0346

Table 1 (*continued*)

Muscle	#	ℓ^f (mm)	ℓ^s (μm)	ℓ^f_o (mm)	ℓ^t (mm)	α (deg)	Mass (g)	PCSA(cm^2)	Origin (bone)	Form	Position (m)			Insertion (bone)	Form	Position (m)		
											x	*y*	*z*			*x*	*y*	*z*
Longissimus thoracis	20	67.0	3.57	50.7	266.3	0	1.40	0.26	L4	Line	−0.0076	−0.0476	0.7410	T4	Point	−0.0279	−0.0896	1.0562
Longissimus thoracis	21	119.8	3.57	90.6	223.3	0	3.83	0.40	L3	Line	−0.0086	−0.0491	0.7572	T3	Point	−0.0239	−0.1049	1.0750
Longissimus thoracis	22	126.0	3.57	95.3	223.6	0	6.06	0.60	L2	Line	−0.0072	−0.0481	0.7772	T2	Point	−0.0209	−0.1211	1.0978
Longissimus thoracis	23	87.0	3.57	65.8	265.5	0	0.91	0.13	L1	Line	−0.0063	−0.0463	0.8014	T1	Point	−0.0222	−0.1453	1.1100
Multifidus	1	55.0	3.35	44.4	12.0	0	0.33	0.07	Sacrum	Surface	−0.0121	−0.0279	0.6555	L5	Point	−0.0082	−0.0457	0.7081
Multifidus	2	47.0	3.35	37.9	21.0	0	0.33	0.08	Sacrum	Surface	−0.0348	−0.0331	0.6513	L5	Point	−0.0100	−0.0506	0.7048
Multifidus	3	51.7	3.35	41.7	55.7	0	2.83	0.64	Sacrum	Surface	−0.0368	−0.0387	0.6333	L4	Point	−0.0065	−0.0485	0.7303
Multifidus	4	42.7	3.35	34.5	41.7	0	1.95	0.54	Sacrum	Surface	−0.0241	−0.0365	0.6528	L4	Point	−0.0061	−0.0541	0.7279
Multifidus	5	42.0	3.35	33.9	27.0	0	0.61	0.17	Sacrum	Surface	−0.0334	−0.0391	0.6747	L4	Point	−0.0083	−0.0612	0.7328
Multifidus	6	38.6	3.35	31.1	72.8	0	4.37	1.33	Sacrum	Surface	−0.0440	−0.0416	0.6489	L3	Point	−0.0091	−0.0511	0.7494
Multifidus	7	34.1	3.35	27.5	28.3	0	1.93	0.66	L5	Surface	−0.0279	−0.0533	0.6990	L3	Point	−0.0099	−0.0580	0.7525
Multifidus	8	27.5	3.35	22.2	19.5	0	0.71	0.30	L5	Point	−0.0350	−0.0652	0.7250	L3	Point	−0.0092	−0.0662	0.7530
Multifidus	9	59.9	3.35	48.3	40.5	0	4.36	0.85	Pelvis	Surface	−0.0407	−0.0526	0.6850	L2	Point	−0.0068	−0.0496	0.7732
Multifidus	10	57.7	3.35	46.6	30.7	0	4.17	0.85	Sacrum	Surface	−0.0237	−0.0518	0.6920	L2	Point	−0.0068	−0.0496	0.7732
Multifidus	11	44.5	3.35	35.9	7.0	0	0.97	0.26	L4	Point	−0.0341	−0.0799	0.7411	L2	Point	−0.0089	−0.0700	0.7759
Multifidus	12	83.4	3.35	67.3	28.0	0	5.27	0.74	Pelvis	Surface	−0.0417	−0.0554	0.6988	L1	Point	−0.0051	−0.0496	0.7983
Multifidus	13	72.7	3.35	58.6	33.8	0	4.74	0.76	L5	Surface	−0.0245	−0.0546	0.6990	L1	Point	−0.0051	−0.0486	0.7983
Multifidus	14	57.3	3.35	46.3	4.7	0	2.37	0.48	L4	Point	−0.0321	−0.0748	0.7456	L1	Point	−0.0036	−0.0553	0.7965
Multifidus	15	30.0	3.35	24.2	11.5	0	0.86	0.34	L3	Point	−0.0242	−0.0838	0.7742	L1	Point	−0.0064	−0.0635	0.8023
Psoas major	1	112.6	2.60	117.1	157.4	0	14.44	1.17	Sacrum	Surface	−0.0356	−0.0939	0.6951	Femur	Line	−0.0818	−0.1022	0.5526
Psoas major	2	112.8	2.60	117.2	223.8	0	21.13	1.70	L3L4IVD	Surface	−0.0280	−0.1080	0.7360	Femur	Line	−0.0818	−0.1022	0.5526
Psoas major	3	138.0	2.60	143.4	201.0	0	11.84	0.78	L3	Surface	−0.0336	−0.0922	0.7600	Femur	Line	−0.0818	−0.1022	0.5526
Psoas major	4	97.5	2.60	101.3	200.5	0	4.68	0.44	L4	Surface	−0.0329	−0.0960	0.7301	Femur	Line	−0.0818	−0.1022	0.5526
Psoas major	5	115.8	2.60	120.4	223.2	0	14.63	1.15	L2	Surface	−0.0260	−0.0909	0.7890	Femur	Line	−0.0818	−0.1022	0.5526
Psoas major	6	126.6	2.60	131.6	226.9	0	38.08	2.74	L1	Surface	−0.0192	−0.0897	0.8199	Femur	Line	−0.0818	−0.1022	0.5526
Psoas major	7	128.4	2.60	133.4	206.6	0	31.76	2.25	L1	Surface	−0.0231	−0.0984	0.8289	Femur	Line	−0.0818	−0.1022	0.5526
Psoas major	8	108.0	2.60	112.2	191.5	0	13.56	1.14	L3	Surface	−0.0248	−0.1085	0.7462	Femur	Line	−0.0818	−0.1022	0.5526
Psoas major	9	131.3	2.60	136.5	206.7	0	11.75	0.81	L2L3IVD	Surface	−0.0270	−0.1150	0.7700	Femur	Line	−0.0818	−0.1022	0.5526
Psoas major	10	136.3	2.60	141.7	211.7	0	12.09	0.81	L2	Surface	−0.0257	−0.1140	0.7784	Femur	Line	−0.0818	−0.1022	0.5526
Quadratus lumborum	1	21.0	2.84	20.0	31.0	0	2.48	1.17	Pelvis	Surface	−0.0791	−0.0783	0.7431	L3	Line	−0.0488	−0.0827	0.7563
Quadratus lumborum	2	26.2	2.84	24.9	29.8	0	0.89	0.34	Pelvis	Surface	−0.0755	−0.0713	0.7428	L2	Line	−0.0493	−0.0791	0.7892
Quadratus lumborum	3	37.4	2.84	35.6	33.6	0	4.00	1.06	Pelvis	Line	−0.0859	−0.0756	0.7434	L2	Line	−0.0491	−0.0799	0.7890
Quadratus lumborum	4	60.7	2.84	57.8	35.3	0	3.06	0.50	Pelvis	Line	−0.0785	−0.0697	0.7427	L1	Point	−0.0433	−0.0757	0.8211
Quadratus lumborum	5	51.4	2.84	48.9	32.1	0	4.85	0.94	L3	Point	−0.0513	−0.0816	0.7607	R12	Line	−0.0425	−0.0700	0.8398
Quadratus lumborum	6	26.3	2.84	25.1	29.7	0	1.99	0.75	Pelvis	Line	−0.0798	−0.0810	0.7410	L3	Point	−0.0513	−0.0825	0.7589
Quadratus lumborum	7	33.0	2.84	31.4	25.5	0	3.07	0.92	Pelvis	Line	−0.0932	−0.0875	0.7439	L2	Line	−0.0491	−0.0799	0.7890
Quadratus lumborum	8	52.0	2.84	49.5	64.0	0	7.81	1.49	Pelvis	Line	−0.1052	−0.0925	0.7430	R12	Line	−0.0466	−0.0702	0.8375
Rectus abdominis	1	262.7	2.72	260.3	50.3	0	28.23	1.13	Pelvis	Surface	−0.0094	−0.1766	0.6040	Sternum	Line	0.0005	−0.2333	0.9028
Rectus abdominis	2	253.3	2.72	251.0	54.2	0	56.19	2.24	Pelvis	Surface	−0.0094	−0.1766	0.6040	R7	Line	−0.0249	−0.2437	0.8972
Rectus abdominis	3	244.3	2.72	242.1	66.7	0	31.53	1.26	Pelvis	Surface	−0.0094	−0.1766	0.6040	R5	Line	−0.0602	−0.2448	0.8992
Serratus posterior inferior	1	27.1	2.74	26.7	98.4	0	1.80	0.64	L1	Line	−0.0047	−0.0447	0.7996	R11	Line	−0.1026	−0.0774	0.8072
Serratus posterior inferior	2	43.2	2.74	42.5	89.8	0	3.39	0.75	T12	Line	−0.0064	−0.0397	0.8387	R10	Line	−0.1119	−0.0818	0.8384
Serratus posterior inferior	3	53.3	2.74	52.4	98.3	0	3.79	0.68	T10	Line	−0.0071	−0.0360	0.8774	R9	Line	−0.1187	−0.0907	0.8732

Transversus abdominus	1	47.5	2.83	45.2	69.0	0	1.36	0.28	Pelvis	Line	−0.1146	−0.1588	0.6950	Linea alba	Line	0.0000	−0.2005	0.6147
Transversus abdominus	2	56.5	2.83	53.8	89.5	0	1.36	0.24	Pelvis	Line	−0.1157	−0.1100	0.7359	Linea alba	Line	0.0000	−0.2086	0.6368
Transversus abdominus	3	112.0	2.83	106.7	159.8	10	2.91	0.25	L4	Line	−0.0484	−0.0828	0.7386	Linea alba	Line	0.0000	−0.2147	0.6648
Transversus abdominus	4	115.0	2.83	109.5	157.3	10	2.91	0.25	L3	Line	−0.0454	−0.0808	0.7590	Linea alba	Line	0.0000	−0.2192	0.6967
Transversus abdominus	5	115.0	2.83	109.5	161.1	10	2.91	0.25	L2	Line	−0.0463	−0.0787	0.7900	Linea alba	Line	0.0000	−0.2225	0.7306
Transversus abdominus	6	105.0	2.83	100.0	168.7	10	2.91	0.27	L1	Line	−0.0396	−0.0745	0.8240	Linea alba	Line	0.0000	−0.2251	0.7646
Transversus abdominus	7	50.0	2.83	47.6	65.8	10	1.96	0.38	R11	Line	−0.1195	−0.1054	0.7761	Linea alba	Line	0.0000	−0.2276	0.7966
Transversus abdominus	8	49.0	2.83	46.7	43.6	10	1.96	0.39	R10	Line	−0.1216	−0.1643	0.7738	Linea alba	Line	0.0000	−0.2303	0.8247
Transversus abdominus	9	35.0	2.83	33.3	24.7	10	1.96	0.55	R9	Line	−0.0839	−0.2217	0.8121	Linea alba	Line	0.0000	−0.2338	0.8469
Transversus abdominus	10	20.0	2.83	19.0	27.1	10	1.96	0.96	R7	Line	−0.0464	−0.2393	0.8595	Linea alba	Line	0.0000	−0.2385	0.8614

[1] Musculo-tendon lengths of longissimus thoracis elements were estimated based on their modeled lines-of-action.

[2] Unfortunately, we accidentally removed the superficial fibers of multifidus around the pelvis. The presented morphological parameters for these elements were estimated based on their modeled lines-of-action.

[3] The mathematical definitions of wrapping surfaces for the psoas major, latissimus dorsi, serratus posterior inferior, obliquus externus abdominis, obliquus internus abdominis, rectus abdominis, and transversus abdominis muscles are presented in Appendix A.2, and the via points for the psoas major, longissimus thoracis, iliocostalis lumborum, and the transversus abdominis muscles are given in Appendix A.3.

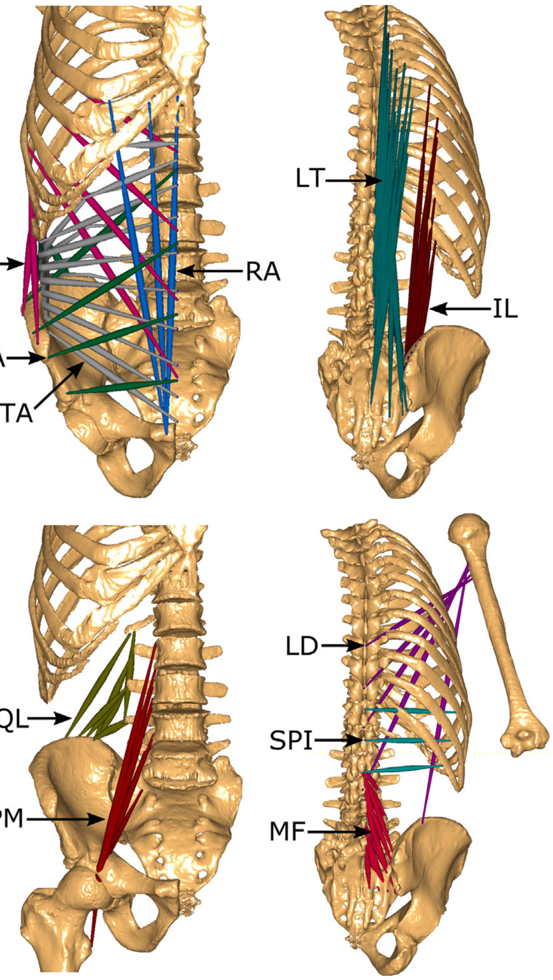

Fig. 3. Dissected muscles in the musculo-skeletal system. OEA: obliquus externus abdominis, OIA: obliquus internus abdominis, TA: transversus abdominis, RA: rectus abdominis, LT: longissimus thoracis, IL: iliocostalis lumborum, QL: quadratus lumborum, PM: psoas major, LD: latissimus dorsi, MF: multifidus, SPI: serratus posterior inferior.

lengths when the muscles were fixed on the skeleton, but a mean shrinkage of 2% when the muscles were fixed in isolation. This implies that sarcomere and fiber lengths measured *in-vitro* may be slightly lower than *in-vivo*. Similarly, measured optimal fiber lengths and physiological cross-sectional areas may change slightly. Fourthly, this dataset was obtained from an elderly male and thus represents a subject specific model, not a generic one. Therefore, certain care should be allocated if a personalized model is aimed to be built upon this dataset. Fifthly, we represented the mechanical function of large muscles by dividing them into a number of muscle-tendon elements. This method simplified the complex function of skeletal muscles and made it suitable to implement in musculo-skeletal models. It is important to emphasize that this approach was a modeling procedure in itself and required some assumptions. The details and underlying assumptions of this method were previously described (van der Helm and Veenbaas, 1991).

Laser diffraction is an accurate method for measuring sarcomere length in skeletal muscle fibers (Cross et al., 1981). We used this method to calculate an average sarcomere length for every muscle and hence to estimate optimal fiber lengths, and PCSAs of its elements. Measured mean sarcomere lengths varied from 2.14 μm to 3.57 μm, which is consistent with the data from Walker and Schrodt (1974). Overall mean and standard deviation on the mean sarcomere lengths were 2.79 ± 0.41 μm, implying that

Table 2
Comparison of the muscle morphological parameters measured in the present study with other anatomical studies.

Muscle	PCSA (cm^2)		ℓ_o^f (cm)		ℓ^s (μm)	
	Present	Other	Present	Other	Present	Other
Obliquus externus abdominis	8.95	5.8 ± 0.7[c]	8.8 ± 3.0	14.6 ± 1.0[c]	2.82	3.18 ± 0.11[c]
Iliocostalis lumborum	6.07	5.47[a], 4.1 ± 1.9[d]	9.9 ± 1.2	14.2 ± 2.1[d]	2.81	2.37 ± 0.17[d], 2.19 ± 0.04[i]
Obliquus internus abdominis	8.30	8.6 ± 0.8[c]	7.3 ± 2.1	7.8 ± 0.4[c]	2.14	2.61 ± 0.06[c]
Latissimus dorsi	6.16	5.6 ± 0.5[e], 8.64 ± 3.05[h]	24.6 ± 3.0	26.4 ± 1.0[e]	2.26	2.69 ± 0.06[e]
Longissimus thoracis	18.50	16.08[a], 5.9 ± 2.5[d]	6.4 ± 1.9	11.7 ± 2.1[d]	3.57	2.31 ± 0.17[d], 2.17 ± 0.03[i]
Multifidus	8.08	8.42[a], 23.9 ± 3.0[k]	4.0 ± 1.2	5.7 ± 0.7[k]	3.35	2.06 ± 0.03[i], 2.27 ± 0.06[k]
Psoas major	12.99	14.63[b], 18.45 ± 4.7[g], 7.7 ± 2.3[j]	12.5 ± 1.4	12.69 ± 2.0[g], 11.69 ± 1.66[j]	2.60	3.03 ± 0.3[g], 3.11 ± 0.28[j]
Quadratus lumborum	7.18	2.8[d]	3.7 ± 1.4	7.1[d]	2.84	2.38[d]
Rectus abdominis	4.63	3.3 ± 0.5[c], 2.6 ± 0.9[d]	25.1 ± 0.9	26.7 ± 1.6[c], 28.0 ± 4.2[d]	2.72	3.29 ± 0.07[c], 2.83 ± 0.28[d]
Serratus posterior inferior	2.07	[f]	4.1 ± 1.3	[f]	2.74	[f]
Transversus abdominus	3.83	5.2 ± 0.7[c]	6.7 ± 3.5	9.7 ± 0.4[c]	2.83	2.58 ± 0.05[c]

[a] Bogduk et al. (1992a), eight adult human cadavers embalmed in a supine position. PCSA was calculated by dividing the volume of each fascicle by its length. Only PCSA of iliocostalis lumborum pars thoracis was shown in the table. PCSA of iliocostalis lumborum pars lumborum was reported as 6.33 cm^2.
[b] Bogduk et al. (1992b), three embalmed human adult male cadavers aged in excess of 60 years. PCSA was calculated by dividing the volume of each fascicle by its length. For comparison, PCSA of each fascicle was summed.
[c] (Brown et al., 2011), five male (mean ± standard deviation age = 71.8 ± 17.9 years, height = 174.8 ± 6.6 cm, mass = 67.8 ± 9.4 kg) and six female (82.7 ± 14.5 years, height = 165.6 ± 3.7 cm, mass = 63.1 ± 11.8 kg) embalmed human cadavers.
[d] Delp et al. (2001), four unembalmed and one embalmed human cadavers (two males and three females, mean ± standard deviation age = 67.0 ± 9.1 years, height = 170.6 ± 4.2 cm, mass = 76.2 ± 13.3 kg). For comparison purposes, PCSAs of the proximal and distal parts were summed, and sarcomere and optimal fiber lengths were averaged between the parts. optimal fiber length was assumed to be 2.8 μm.
[e] Gerling and Brown (2013), twelve embalmed human cadavers (nine males, three females, mean ± standard deviation age = 63.0 ± 11.0 years).
[f] Not available.
[g] Regev et al. (2011), thirteen human cadavers (mean ± standard deviation age = 50.0 ± 6.0 years).
[h] Veeger et al. (1991), five males and two females embalmed human cadavers (mean ± standard deviation age = 80.0 ± 7.0 years, height = 171.1 ± 6.9 cm, mass = 76.1 ± 16.4 kg).
[i] Ward et al. (2009b). Muscle specimens were obtained from patients, iliocostalis lumborum ($n = 7$), longissimus ($n = 7$), and multifidus ($n = 23$).
[j] Ward et al. (2009c), nineteen embalmed human male and female specimens.
[k] Ward et al. (2009a), eight human cadaveric specimens of both genders, (mean ± standard deviation age = 84.0 ± 3.0 years, height = 170.5 ± 11.1 cm, mass = 81.1 ± 15.3 kg).

muscles measured in this study were close to their optimal lengths (~2.7 μm). There exists evidence that the distribution of sarcomere lengths within a muscle fiber is not uniform (Infantolino et al., 2010). Previous studies elaborated on the needed sample size to effectively calculate a mean sarcomere length for a muscle and the effect of sample size on optimal fiber length variation. Langenderfer et al. (2004) showed for the shoulder and elbow muscles that the standard deviation of mean optimal muscle length was about 1.25 mm for 120 samples and increased to nearly 4 mm for 10 samples. Our measurements also confirmed the non-uniform nature of sarcomere length distributions within the muscle fibers. We performed 18 sarcomere length measurements (6 samples × 3 measurements). Therefore, the optimal fiber lengths and PCSAs presented in this paper should be regarded with similar variation. Furthermore, we compared morphological parameters such as PCSAs, optimal fiber lengths, and sarcomere lengths, measured in this study with similar anatomical studies in Table 2. The data reported in the literature indicates some variations for these parameters, especially for PCSAs of the longissimus thoracis, latissimus dorsi, multifidus, and psoas major muscles. Although, in general, we found similar sarcomere lengths with the other studies, we systematically calculated relatively shorter optimal fiber lengths in the present study. The comparison of the fiber lengths revealed lower fiber lengths compared to the other studies. This was attributed to the differences between the heights of the cadavers measured (154 cm in this study and around 170 cm in others). Other reasons which led to such differences may be due to differences in the measurement techniques and the number of samples used for sarcomere length measurements. Moreover, our PCSAs fit with the range of data reported in literature.

In the last decade, the demand for individualized musculoskeletal models has considerably increased aiming to improve the quality of patient specific treatment options. The state-of-the-art approach to obtain personalized models is to morph the medical images of a person to a previously built atlas containing muscle tendon attachment sites and lines-of-action (Pellikaan et al., 2014; Carbone et al., 2015). However, employing such an approach to create personalized models of the spine may only be reasonable up to some degree due to the high variability of muscle attachments with the bones. In this sense, imaging modalities should be improved to help more with creation of such models enabling identification of muscle attachments and obtaining muscle architectural parameters from living subjects (Blemker et al., 2007; Bruno et al., 2015). This objective is definitely one of the future challenges in musculo-skeletal modeling. Meanwhile, we hope that the dataset reported hereby will be a great value to researchers in the field.

Conflict of interest statement

None of the authors have any financial or personal relationships with other people or organization that could inappropriately influence their work.

Acknowledgments

We gratefully acknowledge the financial supports by fonds NutsOhra and the European Research Council 'the BiomechTools project'. We also like to thank several colleagues for their help on this research, Vincenzo Carbone and Kenan Niu for great discussions on musculo-skeletal modeling and working with motion capture systems, Frans Segerink for providing a laser for sarcomere length measurements, Andre Sprengers for his help during CT and MRI scans, and Radiology Department and the Anatomy Department of the Radboud university medical center for their hospitality during the medical imaging and cadaveric measurement sessions. Furthermore, we thank Huub Maas from VU University of Amsterdam for his advice on laser diffraction method.

Appendix A. Supplementary data

Supplementary data associated with this article can be found in the online version at http://dx.doi.org/10.1016/j.jbiomech.2017.01.009.

References

Alireza, A., Weisse, B., Ferguson, S.J., 2011. A multibody modelling approach to determine load sharing between passive elements of the lumbar spine. Comput. Methods Biomech. Biomed. Eng. 14 (6), 527–537.

Arjmand, N., Gagnon, D., Plamondon, A., Shirazi-Adl, A., LariviÃère, C., 2009. Comparison of trunk muscle forces and spinal loads estimated by two biomechanical models. Clin. Biomech. 24 (7), 533–541.

Besl, P.J., McKay, N.D., 1992. A method for registration of 3-d shapes. IEEE Trans. Pattern Anal. Mach. Intell. 14 (February (2)).

Blemker, S.S., Asakawa, D.S., Gold, G.E., Delp, S.L., 2007. Image-based musculoskeletal modeling: applications, advances, and future opportunities. J. Magn. Reson. imaging 25 (2), 441–451.

Bogduk, N., Johnson, G., Spalding, D., 1998. The morphology and biomechanics of latissimus dorsi. Clin. Biomech. 13 (6), 377–385.

Bogduk, N., Macintosh, J.E., Pearcy, M.J., 1992a. A universal model of the lumbar back muscles in the upright position. Spine 17 (8), 897–913.

Bogduk, N., Pearcy, M., Hadfield, G., 1992b. Anatomy and biomechanics of psoas major. Clin. Biomech. 7 (2), 109–119.

Borst, J., Forbes, P.A., Happee, R., Veeger, D.H., 2011. Muscle parameters for musculoskeletal modelling of the human neck. Clin. Biomech. 26 (4), 343–351.

Breteler, M., Spoor, C., Van der Helm, F., 1999. Measuring muscle and joint geometry parameters of a shoulder for modeling purposes. J. Biomech. 32 (11), 1191–1197.

Brown, S., Ward, S., Cook, M., Lieber, R., 2011. Architectural analysis of human abdominal wall muscles: implications for mechanical function. Spine 36 (5), 355–362.

Bruno, A.G., Bouxsein, M.L., Anderson, D.E., 2015. Development and validation of a musculoskeletal model of the fully articulated thoracolumbar spine and rib cage. J. Biomech. Eng. 137 (8) (081003-081003-10).

Bustami, F., 1986. A new description of the lumbar erector spinae muscle in man. J. Anat. 144, 81–91.

Carbone, V., Fluit, R., Pellikaan, P., van der Krogt, M., Janssen, D., Damsgaard, M., Vigneron, L., Feilkas, T., Koopman, H., Verdonschot, N., 2015. Tlem 2.0 - a comprehensive musculoskeletal geometry dataset for subject-specific modeling of lower extremity. J. Biomech. 48 (5), 734–741.

Carbone, V., Van der Krogt, M., Koopman, H., Verdonschot, N., 2012. Sensitivity of subject-specific models to errors in musculo-skeletal geometry. J. Biomech. 45 (14), 2476–2480.

Christophy, M., Faruk Senan, N.A., Lotz, J.C., O'Reilly, O.M., 2012. A musculoskeletal model for the lumbar spine. Biomech. Model. Mechanobiol. 11 (1), 19–34.

Cross, H., West, R., Dutson, T., 1981. Comparison of methods for measuring sarcomere length in beef semitendinosus muscle. Meat Sci. 5 (4), 261–266.

Cutts, A., 1988. Shrinkage of muscle fibres during the fixation of cadaveric tissue. J. Anat. 160, 75–78.

Dao, T.T., Tho, M.-C.H.B., 2015. Assessment of parameter uncertainty in rigid musculoskeletal simulation using a probabilistic approach. J. Musculoskelet. Res. 18 (3), 1550013.

de Zee, M., Hansen, L., Wong, C., Rasmussen, J., Simonsen, E.B., 2007. A generic detailed rigid-body lumbar spine model. J. Biomech. 40 (6), 1219–1227.

Delp, S.L., Suryanarayanan, S., Murray, W.M., Uhlir, J., Triolo, R.J., 2001. Architecture of the rectus abdominis, quadratus lumborum, and erector spinae. J. Biomech. 34 (3), 371–375.

der Helm, F.V., Veeger, H., Pronk, G., der Woude, L.V., Rozendal, R., 1992. Geometry parameters for musculoskeletal modelling of the shoulder system. J. Biomech. 25 (2), 129–144.

Gerling, M., Brown, S., 2013. Architectural analysis and predicted functional capability of the human latissimus dorsi muscle. J. Anat. 223 (2), 112–122.

Ignasiak, D., Dendorfer, S., Ferguson, S., 2016. Thoracolumbar spine model with articulated ribcage for the prediction of dynamic spinal loading. J. Biomech. 49 (6), 959–966.

Infantolino, B., Ellis, M., Challis, J., 2010. Individual sarcomere lengths in whole muscle fibers and optimal fiber length computation. Anat. Rec. 293 (11), 1913–1919.

Kamibayashi, L., Richmond, F., 1998. Morphometry of human neck muscles. Spine 23 (12), 1314–1323.

Klein Horsman, M., Koopman, H., van der Helm, F., ProsÃl', L., Veeger, H., 2007. Morphological muscle and joint parameters for musculoskeletal modelling of the lower extremity. Clin. Biomech. 22 (2), 239–247.

Langenderfer, J., Jerabek, S., Thangamani, V., Kuhn, J., Hughes, R., 2004. Musculoskeletal parameters of muscles crossing the shoulder and elbow and the effect of sarcomere length sample size on estimation of optimal muscle length. Clin. Biomech. 19 (7), 664–670.

Macintosh, J.E., Bogduk, N., 1987. 1987 volvo award in basic science: the morphology of the lumbar erector spinae. Spine 12 (7), 658–668.

Macintosh, J.E., Bogduk, N., 1991. The attachments of the lumbar erector spinae. Spine 16 (7), 783–792.

Macintosh, J.E., Valencia, F., Bogduk, N., Munro, R.R., 1986. The morphology of the human lumbar multifidus. Clin. Biomech. 1 (4), 196–204.

Mahato, N., 2013. Pars inter-articularis and laminar morphology of the terminal lumbar vertebra in lumbosacral transitional variations. North Am. J. Med. Sci. 5 (6), 357–361.

McGill, S.M., 1992. A myoelectrically based dynamic three-dimensional model to predict loads on lumbar spine tissues during lateral bending. J. Biomech. 25 (4), 395–414.

Pellikaan, P., van der Krogt, M., Carbone, V., Fluit, R., Vigneron, L., Van Deun, J., Verdonschot, N., Koopman, H., 2014. Evaluation of a morphing based method to estimate muscle attachment sites of the lower extremity. J. Biomech. 47 (5), 1144–1150.

Phillips, S., Mercer, S., Bogduk, N., 2008. Anatomy and biomechanics of quadratus lumborum. Proc. Inst. Mech. Eng. Part H: J. Eng. Med. 222 (2), 151–159.

Putzer, M., Ehrlich, I., Rasmussen, J., Gebbeken, N., Dendorfer, S., 2016. Sensitivity of lumbar spine loading to anatomical parameters. J. Biomech. 49 (6), 953–958.

Regev, G., Kim, C., Tomiya, A., Lee, Y., Ghofrani, H., Garfin, S., Lieber, R., Ward, S., 2011. Psoas muscle architectural design, in vivo sarcomere length range, and passive tensile properties support its role as a lumbar spine stabilizer. Spine 36 (26), E1666–E1674.

van der Helm, F., Veenbaas, R., 1991. Modelling the mechanical effect of muscles with large attachment sites: application to the shoulder mechanism. J. Biomech. 24 (12), 1151–1163.

Vasavada, A.N., Li, S., Delp, S.L., 1998. Influence of muscle morphometry and moment arms on the moment-generating capacity of human neck muscles. Spine 23 (4), 412–422.

Veeger, H., Van Der Helm, F., Van Der Woude, L., Pronk, G., Rozendal, R., 1991. Inertia and muscle contraction parameters for musculoskeletal modelling of the shoulder mechanism. J. Biomech. 24 (7), 615–629.

Walker, S., Schrodt, G., 1974. I segment lengths and thin filament periods in skeletal muscle fibers of the rhesus monkey and the human. Anat. Rec. 178 (1), 63–81.

Ward, S., Kim, C., Eng, C., Gottschalk IV, L., Tomiya, A., Garfin, S., Lieber, R., 2009a. Architectural analysis and intraoperative measurements demonstrate the unique design of the multifidus muscle for lumbar spine stability. J. Bone Jt. Surg. - Ser. A 91 (1), 176–185.

Ward, S., Tomiya, A., Regev, G., Thacker, B., Benzl, R., Kim, C., Lieber, R., 2009b. Passive mechanical properties of the lumbar multifidus muscle support its role as a stabilizer. J. Biomech. 42 (10), 1384–1389.

Ward, S.R., Eng, C.M., Smallwood, L.H., Lieber, R.L., 2009c. Are current measurements of lower extremity muscle architecture accurate? Clin. Orthop. Relat. Res. 467 (4), 1074–1082.

Wilke, H.-J., Kienle, A., Maile, S., Rasche, V., Berger-Roscher, N., 2016. A new dynamic six degrees of freedom disc-loading simulator allows to provoke disc damage and herniation. Eur. Spine J. 25 (5), 1363–1372.

Zajac, F., 1989. Muscle and tendon: properties, models, scaling, and application to biomechanics and motor control. Crit. Rev. Biomed. Eng. 17 (4), 359–411.

Zander, T., Dreischarf, M., Schmidt, H., Bergmann, G., Rohlmann, A., 2015. Spinal loads as influenced by external loads: a combined in vivo and in silico investigation. J. Biomech. 48 (4), 578–584.